



# Nonlinear absorption and integrated photonics applications of MoSSe

XIAOBO LI,<sup>1,2</sup> XIN CHEN,<sup>1,2</sup> NING WEI,<sup>1,2</sup> CHENDUAN CHEN,<sup>1,2</sup>  
ZHAN YANG,<sup>1,2</sup> HAIJIAO XIE,<sup>3</sup> JIAJING HE,<sup>1,4,5</sup>   
NINGNING DONG,<sup>1,2,4,6</sup> YAPING DAN,<sup>5</sup> AND JUN WANG<sup>1,2,4,6,\*</sup>

<sup>1</sup>Laboratory of Micro-Nano Optoelectronic Materials and Devices, Key Laboratory of Materials for High-Power Laser, Shanghai Institute of Optics and Fine Mechanics, Chinese Academy of Sciences, Shanghai 201800, China

<sup>2</sup>Center of Materials Science and Optoelectronics Engineering, University of Chinese Academy of Sciences, Beijing 100049, China

<sup>3</sup>Hangzhou Yanqu Information Technology, Hangzhou, Zhejiang 310003, China

<sup>4</sup>CAS Center for Excellence in Ultra-intense Laser Science (CEULS), Shanghai 201800, China

<sup>5</sup>University of Michigan–Shanghai Jiao Tong University Joint Institute, Shanghai Jiao Tong University, Shanghai 200240, China

<sup>6</sup>State Key Laboratory of High Field Laser Physics, Shanghai Institute of Optics and Fine Mechanics, Chinese Academy of Sciences, Shanghai 201800, China

\*[jwang@siom.ac.cn](mailto:jwang@siom.ac.cn)

**Abstract:** This study explores the wavelength-dependent and pulse-width-dependent nonlinear optical properties of liquid-phase exfoliated molybdenum sulfide selenide (MoSSe) nanosheets. The saturable absorption response of MoSSe nanosheets in the visible region is better than that in the near-infrared region, and the response under 6-ns pulse excitation is better than that of a 380-fs pulse. Furthermore, based on the first-principles calculations, we designed a phase modulator and optimized its structure by integrating a monolayer MoSSe into a silicon slot waveguide. The simulation results revealed that the phase shift could achieve a high optical extinction. Consequently, MoSSe exhibits satisfactory nonlinear optical properties and an excellent potential for applications in optoelectronic devices.

© 2022 Optica Publishing Group under the terms of the [Optica Open Access Publishing Agreement](#)

## 1. Introduction

Two-dimensional (2D) materials represented by graphene and transition metal dichalcogenides (TMDs) have outstanding optical, electrical, and mechanical properties, and a great potential in flexible photonics, terahertz technology, quantum optics, microwave photonics and other fields [1–7]. In recent years, the combination of 2D materials with integrated photonic systems has garnered wide attention, particularly in optical modulators [8–10]. Optical modulators are the key components of the high-speed optical signal processing, including all-optical, electro-optical, acousto-optical, thermal-optical and other types, of which electro-optical modulators are the most commonly used type [11–15]. Electro-optical modulators based on 2D materials are fabricated using the tunability of electrostatic doping of 2D materials. Many existing studies on electro-optical modulators based on 2D materials have focused on graphene; however, limited studies have been conducted on TMD electro-optical modulators, and even less on TMD electro-optical modulators operating at a wavelength of 1550 nm [16–19]. Although the refraction and absorption of TMDs can be simultaneously tuned by voltage near the exciton resonance, the light absorption near the exciton resonance is extremely large, and the wavelength is not located at the ordinary communication band, which limits its application [20–24]. To extend the application of TMDs to the communication frequency band, a feasible solution is to design it as a phase modulator using the electro-refractive effect.

In addition to conventional TMDs of binary elements, emerging alloys of ternary TMDs have also garnered considerable attention, such as WSSe, MoSSe, etc [25]. Molybdenum sulfide selenide (MoSSe) is a ternary TMD alloy with a similar structure to MoS<sub>2</sub>, with a Mo layer sandwiched between the S and Se layers. MoSSe possesses new physical properties, such as higher lattice thermal conductivity, greater carrier mobility, and enhanced piezoelectric effect, owing to the breaking of the symmetry of the MoS<sub>2</sub> structure and existence of out-of-plane dipoles [26,27]. However, current studies on the optical and electrical properties of MoSSe are mostly based on theoretical analyses, lacking experimental confirmation of its unique properties. In addition, combinations of MoSSe with on-chip optical modulators need further investigations. To solve these problems, we experimentally verified the nonlinear optical properties of MoSSe, and obtained the linear dielectric constant by first-principles calculations, followed by modulator simulations.

In this study, we prepared MoSSe nanosheets using a liquid-phase exfoliation technique and characterized the quality of resulting nanosheets using the UV-visible absorption spectroscopy,

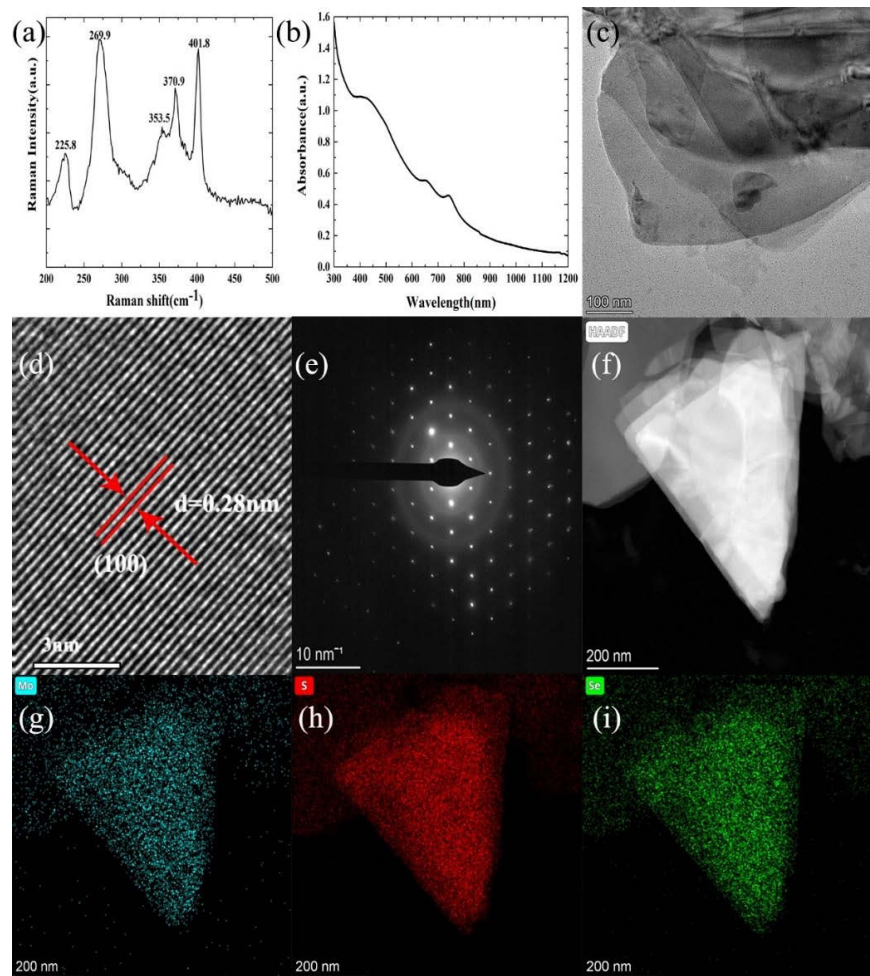


**Fig. 1.** (a) Raman spectra of MoSSe nanosheets on sapphire substrates. (b) Absorption spectra of MoSSe dispersions in NMP. (c) TEM images, (d) HRTEM images, (e) SAED images of MoSSe nanosheets. (f) Typical HAADF-STEM image, and corresponding mappings for (g) Mo, (h) S, and (i) Se elements.

Raman spectroscopy, and Transmission electron microscopy (TEM). The NLO responses of MoSSe nanosheets excited by 1040/520 nm femtosecond (fs) pulses and 1064/532 nm nanosecond (ns) pulses were investigated using the open-aperture Z-scan technique. Subsequently, the experimental results were fitted with the corresponding fast and slow saturable absorption (SA) models to verify the NLO performance of MoSSe nanosheets. Finally, we applied MoSSe to an on-chip optical modulator, designed and optimized a slot-waveguide-based phase modulator based on the results obtained using the first-principles calculations, proving that MoSSe could have potential applications as the optical modulators.

## 2. Material characterization

In this study, we prepared MoSSe dispersions in N-methylpyrrolidone (NMP) using a practical liquid-phase exfoliation technique, followed by a series of characterizations to confirm the high quality of the nanosheets. The Raman spectrum in Fig. 1(a) shows that the prepared MoSSe nanosheets had five distinct peaks at 225.8, 269.9, 353.5, 370.9 and 401.8  $\text{cm}^{-1}$ , respectively. Figure 1(b) shows the absorption spectrum of the MoSSe nanosheets, which exhibited a decreasing trend from 300 to 1200 nm, with absorption peaks at 400, 647, and 739 nm. The morphology of the prepared MoSSe nanosheets was characterized using TEM at a scale of 100 nm, as shown in Fig. 1(c). Furthermore, the in-plane high-resolution TEM images and selected area electron diffraction (SAED) patterns of MoSSe are shown in Figs. 1(d) and 1(e), respectively, from which a lattice constant of 0.28 nm along the (100) direction can be obtained. A high-angle annular dark-field scanning TEM image of MoSSe (STEM-HAADF) is shown in Fig. 1(f), it can be clearly seen that the sample has few layers. A uniform distribution of Mo, S, and Se elements with an elemental ratio of approximately 1:1:1 can be obtained from the elemental energy dispersive X-ray spectroscopy (EDS) images, as shown in Figs. 1(g)-(i).

## 3. Nonlinear optical performance

In order to measure the NLO properties, we used the open-aperture Z-scan technique [28–30]. The MoSSe dispersions were placed in a  $10 \times 10$  mm quartz cuvette, and the linear transmittances were 35.56% at 532 nm, 68.03% at 1064 nm, 23.72% at 520 nm, and 65.10% at 1040 nm, respectively. Figure 2 shows the normalized transmission of the MoSSe nanosheets under different excitation sources. Under the excitation of 6-ns and 380-fs laser pulses, the normalized transmission peak gradually increased with an increase in the input laser pulse energy, and the normalized transmission exhibited a symmetrical peak around the lens focus, indicating a typical SA response owing to Pauli-blocking principles. It is worth mentioning that we did not observe any obvious signal in the pure NMP solvent in our experiments, implying that the SA response was mainly from the MoSSe nanosheets.

We fit these Z-scan results using the propagation equation as follows [30]:

$$\frac{dI(z')}{dz'} = -\alpha(I)I. \quad (1)$$

where  $I$  is the incident light intensity,  $Z'$  is the propagation depth in the material, and the total absorption  $\alpha(I)$  can be obtained from the linear absorption coefficient  $\alpha_0$  and nonlinear absorption coefficient  $\alpha_{NL}$  as follows:

$$\alpha(I) = \alpha_0 + \alpha_{NL}I. \quad (2)$$

To obtain the SA intensity ( $I_{sat}$ ), we fitted the results of the ns laser excitation using an SA model  $\alpha(I) = \alpha_0 / (1 + I/I_{sat})$ . The described SA model can only be used for steady-state two-level systems [31]. That is, the excitation pulse width should be considerably longer than the in-band relaxation time, such that the excited electrons in the conduction band have sufficient time to achieve band filling. The inter-band relaxation time of MoSSe is of the order of picoseconds

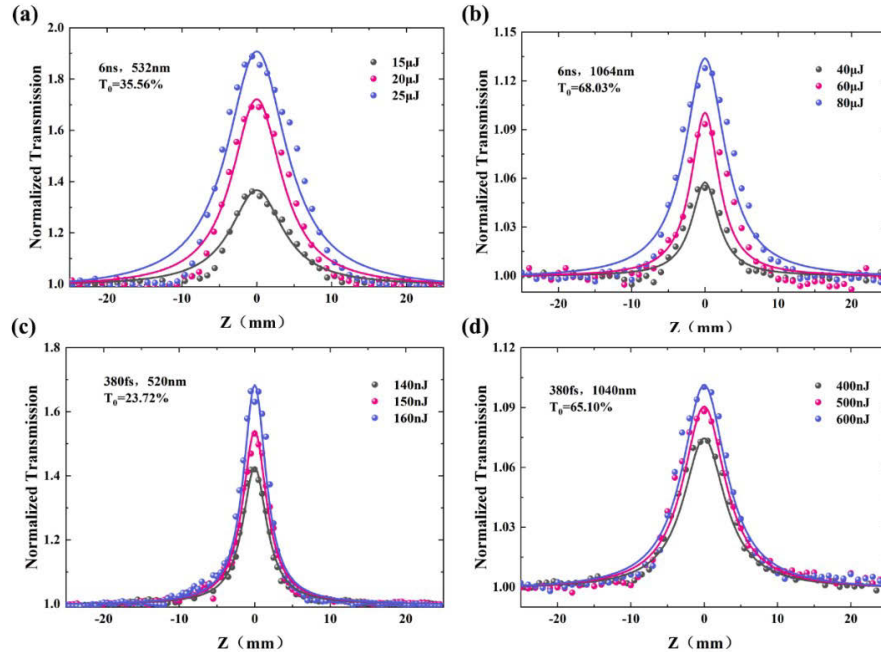


**Fig. 2.** Z-scan results of MoS<sub>2</sub> dispersions under nanosecond pulse excitations at (a) 532 nm and (b) 1,064 nm and femtosecond pulse excitation at (c) 520 nm and (d) 1,040 nm. The solid lines represent the corresponding fitting results.

[25]. Therefore, the above formula can only be used to estimate  $I_{sat}$  under a 6-ns pulse excitation. For an  $I_{sat}$  excited by a 380-fs pulse, it can be calculated using  $I_{sat} = \hbar\omega/\sigma\tau_p$ , where  $\sigma$  is the absorption cross-section and  $\hbar\omega$  is the energy of the incident photon [32]. The fitting results are shown in Table 1.

**Table 1. Linear and nonlinear optical parameters of MoS<sub>2</sub> dispersion.**

pulse width	$\lambda$ (nm)	$T_0$ (%)	$\alpha_0$ (cm <sup>-1</sup> )	$\alpha_{NL}$ (cm/GW)	$Im\chi^{(3)}$ (esu)	FOM (esu cm)	$I_{sat}$ (GW/cm <sup>2</sup> )
6-ns	1064	68.03	0.385	$-0.31 \pm 0.07$	$-(5.95 \pm 1.35) \times 10^{-13}$	$(1.55 \pm 0.35) \times 10^{-12}$	$1.19 \pm 0.17$
6-ns	532	35.56	1.034	$-5.76 \pm 0.86$	$-(6.17 \pm 0.92) \times 10^{-12}$	$(5.96 \pm 0.89) \times 10^{-12}$	$0.18 \pm 0.03$
380fs	1040	65.10	0.429	$-(2.83 \pm 0.31) \times 10^{-3}$	$-(5.35 \pm 0.63) \times 10^{-15}$	$(1.25 \pm 0.15) \times 10^{-14}$	$113.22 \pm 1.87$
380fs	520	23.72	1.439	$-(2.07 \pm 0.16) \times 10^{-2}$	$-(1.92 \pm 0.15) \times 10^{-14}$	$(1.34 \pm 0.10) \times 10^{-14}$	$47.93 \pm 5.82$

In addition, the imaginary part of the third-order NLO susceptibility ( $Im\chi^{(3)}$ ) can be obtained using  $\alpha_{NL}$ , that is,  $Im\chi^{(3)} = (10^{-7}c\lambda n^2\alpha_{NL})/(96\pi^2)$ , where  $c$ ,  $\lambda$  and  $n$  are the speed of light, wavelength of incident light, and refractive index (obtained from the parallel dielectric constant calculated from the DFT calculations in Section 4), respectively. To eliminate the difference caused by different linear absorption coefficients  $\alpha_0$ , we defined  $FOM = |Im\chi^{(3)}/\alpha_0|$  [20]. The calculated results are listed in Table 1. It can be seen that  $\alpha_{NL}$  and  $Im\chi^{(3)}$  at 532/520 nm are an order of magnitude larger than those at 1064/1040 nm, whereas the trend of  $I_{sat}$  is the opposite, that is, the MoS<sub>2</sub> nanosheets have better SA in the visible range. In addition, the values of  $\alpha_{NL}$ ,  $Im\chi^{(3)}$  and FOM under ns pulse excitations are approximately two orders of magnitude larger

than those under fs pulse excitations, indicating that MoSSe exhibits a higher SA performance under ns pulse excitations. We further investigated the pulse-duration dependence of this SA capacity using fast and slow SA models [33,34].

The excited state absorption (ESA) cross section ( $\sigma_{es}$ ) and ground-state absorption (GSA) cross section ( $\sigma_{gs}$ ) are key parameters for evaluating the quality of saturable absorbers, which can be obtained using the fast and slow SA models. When the inter-band relaxation time was significantly smaller than the pulse duration of the incident light, the fast SA model was adopted. We can obtain the transmittance of the fast absorber by solving the equation below: [33]

$$T \left[ \frac{S + II(0)}{S + I(0)} \right]^D = T_0; S = (\tau\sigma_{gs})^{-1}; D = \frac{\sigma_{gs} - \sigma_{es}}{\sigma_{es}}; T_0 = 1/(e^{(NL\sigma_{gs})}). \quad (3)$$

where  $T_0$ ,  $N$ ,  $L$ , and  $\tau$  are the linear transmittance, absorber density, sample thickness, and inter-band relaxation time, respectively; and  $I(0)$  is the input beam intensity of photons per unit area per unit time. For beams with a transverse Gaussian distribution,  $I(0)$  in Eq. (3) should be replaced with  $I(0)/2$ .

Contrary to the fast SA model, the slow SA model is appropriate for an incident light with a pulse duration shorter than the inter-band relaxation time; its Frantz-Nodvik equation is expressed as follows:

$$T = T_0 + \frac{(T_{FN} - T_0)(T_{\max} - T_0)}{1 - T_0}; T_{\max} = e^{-NL\sigma_{es}}; T_{FN} = \frac{\ln\{1 + T_0[e^{\sigma_{gs}E(0)} - 1]\}}{\sigma_{gs}E(0)}. \quad (4)$$

where  $T_{\max}$  is the theoretically achievable maximum transmittance and  $T_{FN}$  represents the transmittance of an “ideal” saturable absorber ( $\sigma_{es}=0$ ).

Therefore, we fitted the Z-scan experimental results with the 6-ns pulse width with the fast SA model, and the shorter 380-fs pulse width with the slow SA model. The fitting results and parameters are presented in Fig. 3 and Table 2, respectively. The performance of the saturable absorber material can be more accurately evaluated using  $\sigma_{es}/\sigma_{gs}$ , and all its values in Table 2 are less than 1, which is reasonable for SA. The values of  $\sigma_{es}/\sigma_{gs}$  were 0.034 and 0.026 under the ns pulse, and 0.532 and 0.271 under the fs pulse excitations. It is obvious that the value of  $\sigma_{es}/\sigma_{gs}$  under ns pulse is an order of magnitude smaller than that of fs pulse, which indicates that the MoSSe dispersion can easily achieve excited state absorption under a ns pulse excitation. As mentioned above, it is more accurate to use  $\sigma_{es}/\sigma_{gs}$  to measure the SA performance, and the smaller the value of  $\sigma_{es}/\sigma_{gs}$  means that the material has better SA performance, and  $\sigma_{es}/\sigma_{gs}$  does not change much when the wavelengths are similar. Therefore, the SA performance of MoSSe is better than graphene, lower than InSe and BP, and similar to MoS<sub>2</sub> [35–39]. In addition, a smaller  $\sigma_{es}/\sigma_{gs}$  indicates that the behavior of the absorber excited state-filling behavior is similar to that of two-level systems under short pulses, compared to the band filling phenomenon exhibited by a long pulse excitation. Therefore, under a 6-ns pulse excitation, the MoSSe nanosheets reached saturation more easily and had larger  $\alpha_{NL}$ , and the Z-scan results were satisfactorily agreed with fitting parameters of the fast and slow SA models.

**Table 2. Parameters obtained by the fast and slow SA absorber model fittings.**

model	pulse width	wavelength (nm)	$N$ (cm <sup>-3</sup> )	$T_{\max}$	$\sigma_{gs}$ (cm <sup>2</sup> )	$\sigma_{es}$ (cm <sup>2</sup> )	$\sigma_{es}/\sigma_{gs}$
fast	6ns	532	$5.19 \times 10^{17}$	0.965	$1.99 \times 10^{-18}$	$6.80 \times 10^{-20}$	0.034
fast	6ns	1064	$6.30 \times 10^{18}$	0.990	$6.11 \times 10^{-20}$	$1.60 \times 10^{-21}$	0.026
slow	380fs	520	$6.36 \times 10^{15}$	0.465	$2.26 \times 10^{-16}$	$1.20 \times 10^{-16}$	0.532
slow	380fs	1040	$1.79 \times 10^{16}$	0.891	$2.40 \times 10^{-17}$	$6.51 \times 10^{-18}$	0.271

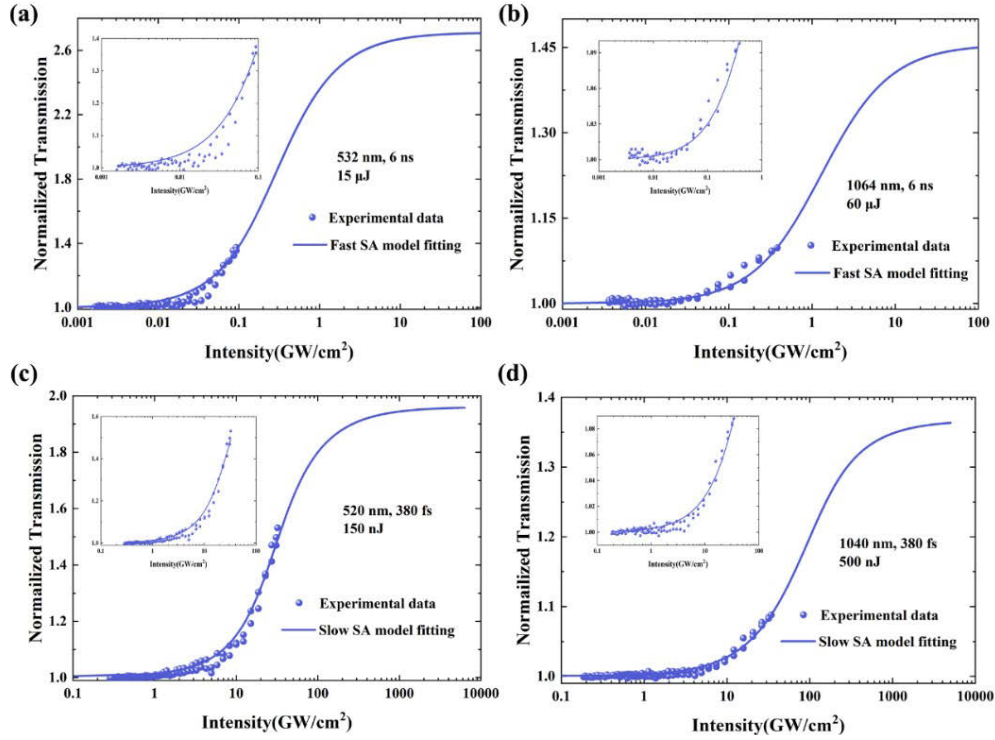


**Fig. 3.** Nonlinear transmission of MoS<sub>2</sub> dispersions depends on the incident light intensity, fitted by a fast SA model (a, b) under ns laser and a slow SA model (c, d) under fs laser.

#### 4. First-principles calculations

The detailed calculation process of single-layer MoS<sub>2</sub> using density functional theory (DFT) can be found in Supplement IV. DFT calculations show that monolayer MoS<sub>2</sub> is a direct-gap semiconductor with a bandgap of 1.55 eV (Supplement 1, Fig. S1). The calculated work function was 5.26 eV (Supplement 1, Fig. S2), which was comparable to the results presented by Mwankemwa et al [40].

Furthermore, we calculated the dielectric constant to reveal its optical properties for potential applications in optoelectronic devices. Moreover, the material is polarized under the electric field of the incident light, and the polarization can be calculated under the approximation of the linear response as follows [41]:

$$P^i(\omega) = \chi_{ij}^{(1)}(-\omega, \omega)E^j(\omega). \quad (5)$$

where  $\chi_{ij}^{(1)}$  is the linear optical susceptibility tensor, which is expressed as follows [42]:

$$\chi_{ij}^{(1)}(-\omega, \omega) = \frac{e^2}{\hbar\Omega} \sum_{nmk} f_{nm}(k) \frac{r_{nm}^i(k)r_{mn}^j(k)}{\omega_{mn}(k) - \omega} = \frac{\varepsilon_{ij}(\omega) - \varepsilon_{ij}}{4\pi}. \quad (6)$$

where  $n$  and  $m$  denote the energy bands,  $f_{nm}(k) = f_n(k) - f_m(k)$  is the Fermi occupation factor,  $\Omega$  is the normalization volume, and  $\omega_{mn}(k) = \omega_m(k) - \omega_n(k)$  are the frequency differences. From Eq. (6), the linear optical susceptibility tensor can be written in two parts: the real part  $\varepsilon_1(\omega)$  and the imaginary part  $\varepsilon_2(\omega)$  of the dielectric function  $\varepsilon(\omega)$ , that is,  $\varepsilon(\omega) = \varepsilon_1(\omega) + i\varepsilon_2(\omega)$ . The real part  $n(\omega)$  and imaginary part  $k(\omega)$  of the refractive index can be obtained using the dynamic

dielectric function  $\varepsilon(\omega)$ . The explicit expression is as follows [43,44]:

$$n(\omega) = \left(\frac{1}{\sqrt{2}}\right) \left[ \sqrt{\varepsilon_1(\omega)^2 + \varepsilon_2(\omega)^2} + \varepsilon_1(\omega) \right]^{\frac{1}{2}}. \quad (7)$$

$$k(\omega) = \left(\frac{1}{\sqrt{2}}\right) \left[ \sqrt{\varepsilon_1(\omega)^2 + \varepsilon_2(\omega)^2} - \varepsilon_1(\omega) \right]^{\frac{1}{2}}. \quad (8)$$

We use theoretical calculations to obtain real and imaginary parts of the frequency-dependent complex dielectric function, and the refractive index can be further extracted. In this calculation, we considered both the parallel and vertical polarized light; and the results are shown in Fig. 4, and the calculated results are consistent with the work of Mwankemwa et al. [40]. The real part of the dielectric constant of a material is related to polarization and anomalous dispersion effects, and the imaginary part determines the absorption of the material [43]. The first optical peak of the imaginary part is located in the visible light region, and its oscillation is owing to the oscillation of the charge distribution caused by the generation of excitons. Below 1.5 eV, the imaginary part of the MoSSe dielectric function is 0; thus, its extinction coefficient  $k$  is 0 in the near-infrared region.

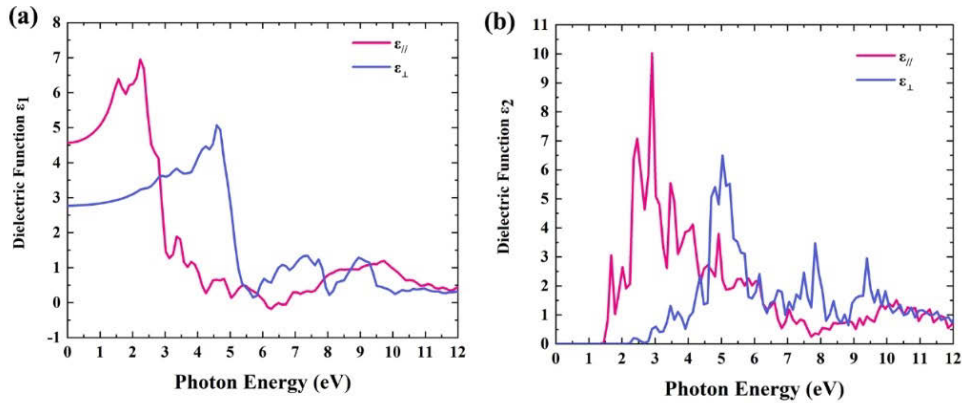


**Fig. 4.** Calculated (a) real and (b) imaginary parts of the MoSSe dielectric function.

## 5. Designing integrated photonic devices

To verify the potential of MoSSe for photonic integration applications, we designed a phase modulator based on monolayer MoSSe, as presented in Figs. 5(a) and 5(b). The modulator consists of silicon dioxide cladding, a slot waveguide made of two identical silicon waveguides, and a parallel-plate capacitor structure above the waveguides. Because TMDs can be completely matched with the hexagonal lattice of hexagonal boron nitride (hBN), hBN was used as a spacer to prevent carrier diffusion. Moreover, it separates ITO from MoSSe to form a slab capacitor [45]. The monolayer MoSSe and bottom silicon waveguide are separated by a 5-nm hBN, while the thickness of hBN between the monolayer MoSSe and ITO is 30 nm, and the thickness of ITO is 5 nm. The width ( $w_{Si}$ ) and height ( $h_{Si}$ ) of the silicon waveguide and width of the slot ( $w_{slot}$ ) need to be optimized. In the subsequent simulations, monolayer MoSSe was modeled as an anisotropic material with a thickness of 0.7 nm. The refractive indices of silicon dioxide, silicon, and hBN were considered as 1.44, 3.47, and 1.98, respectively, while the refractive index of ITO was  $1.76 + 0.07i$  [46]. For monolayer 2D materials, the voltage does not cause a significant change in the out-of-plane dielectric constant  $\varepsilon_{\perp}$ ; however, it has a considerable effect

on the in-plane dielectric constant  $\varepsilon_{\parallel}$ ; thus, we only need to consider changes in  $\varepsilon_{\parallel}$  caused by the voltage [9,47]. Using the first-principles calculations, we obtained  $n_{\parallel}$  and  $n_{\perp}$  of the monolayer MoSSe at a wavelength of 1550 nm as 2.205 and 1.677, respectively. In addition, we performed a simulation analysis of the designed phase modulator using the commercial software Lumerical Solution. Figure 5(c) shows its mode distribution, and the light is well confined in the slot region. Additionally, we can observe that changes in the real part of the refractive indices of WS<sub>2</sub> and MoS<sub>2</sub> caused by voltage are approximately 0.95 and 0.46, respectively, and the effects on the imaginary part are on the order of  $10^{-3}$ , that is, the light propagating in them will produce a significant phase change with an extremely low propagation loss (approximately 0.0132dB/ $\mu\text{m}$  in WS<sub>2</sub>) [46]. Consequently, we directly used changes in the refractive index of MoSSe (induced by voltage) for simulation, assuming that the change in the real part of the MoSSe refractive index ( $\Delta n$ ) is approximately 0.4, and that of the imaginary part ( $\Delta k$ ) is approximately 0.005.

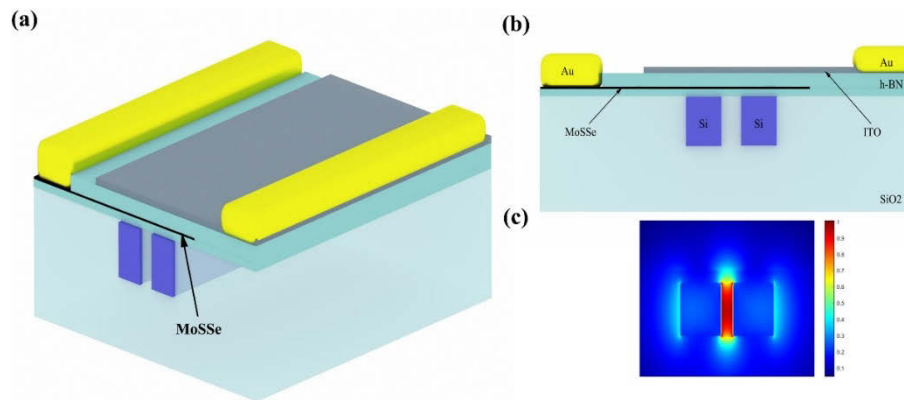


**Fig. 5.** (a) 3D view, (b) cross-section, and (c) electric field of the TE mode of the modulator.

For the phase modulator, we focused on the change in  $\text{Re}(n_{\text{eff}})$ , while the change in  $\Delta k$  had no effect on  $\text{Re}(n_{\text{eff}})$  and only 1.85% on the loss (Supplement 1, V). Therefore, changes in the imaginary part of the MoSSe refractive index can be ignored during changes in its real part. To obtain a better-performing modulator, the structure of the modulator should be optimized to enhance the interaction between the light mode and monolayer MoSSe. For the electro-absorption modulator, the structural parameters should be swept to maximize the absorption [48]; however, for the MoSSe phase modulator, the maximum phase change should be obtained. According to  $\Delta\varphi = 2\pi L \Delta \text{Re}(n_{\text{eff}}) / \lambda$ , we need to maximize  $\Delta \text{Re}(n_{\text{eff}})$  in the case of a certain length  $L$ , which is insignificant to sweep only the structural parameters or only  $\Delta n$ ; thus, nested parameter sweep should be used to obtain the pseudo color map, and then use MATLAB to process the data; the results are shown in Fig. 6. The modulator is realized by adjusting the refractive index of the MoSSe. In addition, to observe  $\Delta \text{Re}(n_{\text{eff}})$  more intuitively, the results in Figs. 6(a), 6(c), and 6(e) present differences between the effective refractive indices of different  $h_{\text{Si}}$ ,  $w_{\text{Si}}$ ,  $w_{\text{slot}}$  and the effective refractive index of  $\Delta n = 0$  for each  $\Delta n$  case. The influence of  $h_{\text{Si}}$  and  $\Delta n$  on  $\Delta \text{Re}(n_{\text{eff}})$  and loss when  $w_{\text{Si}} = 210$  nm and  $w_{\text{slot}} = 60$  nm are shown in Figs. 6(a) and 6(b), respectively. For the phase modulator, the maximum  $\Delta \text{Re}(n_{\text{eff}})$  and minimum loss are needed. Therefore, we chose the height of the silicon waveguide to be 170 nm. The effects of  $w_{\text{Si}}$  and  $\Delta n$  on  $\Delta \text{Re}(n_{\text{eff}})$  and loss when  $h_{\text{Si}} = 170$  nm and  $w_{\text{slot}} = 60$  nm are shown in Figs. 6(c) and 6(d), respectively. To guarantee single-mode transmission conditions, the width of the waveguide should not be extremely large. Considering the above requirements, the width of the silicon waveguide was selected to be 210 nm. When  $h_{\text{Si}} = 170$  nm and  $w_{\text{Si}} = 210$  nm, the effects of slot width  $w_{\text{slot}}$  and

$\Delta n$  on  $\Delta \text{Re}(n_{\text{eff}})$  and loss are illustrated in Figs. 6(e) and 6(f), respectively. Considering all above factors comprehensively, the slot width was chosen to be 30 nm.

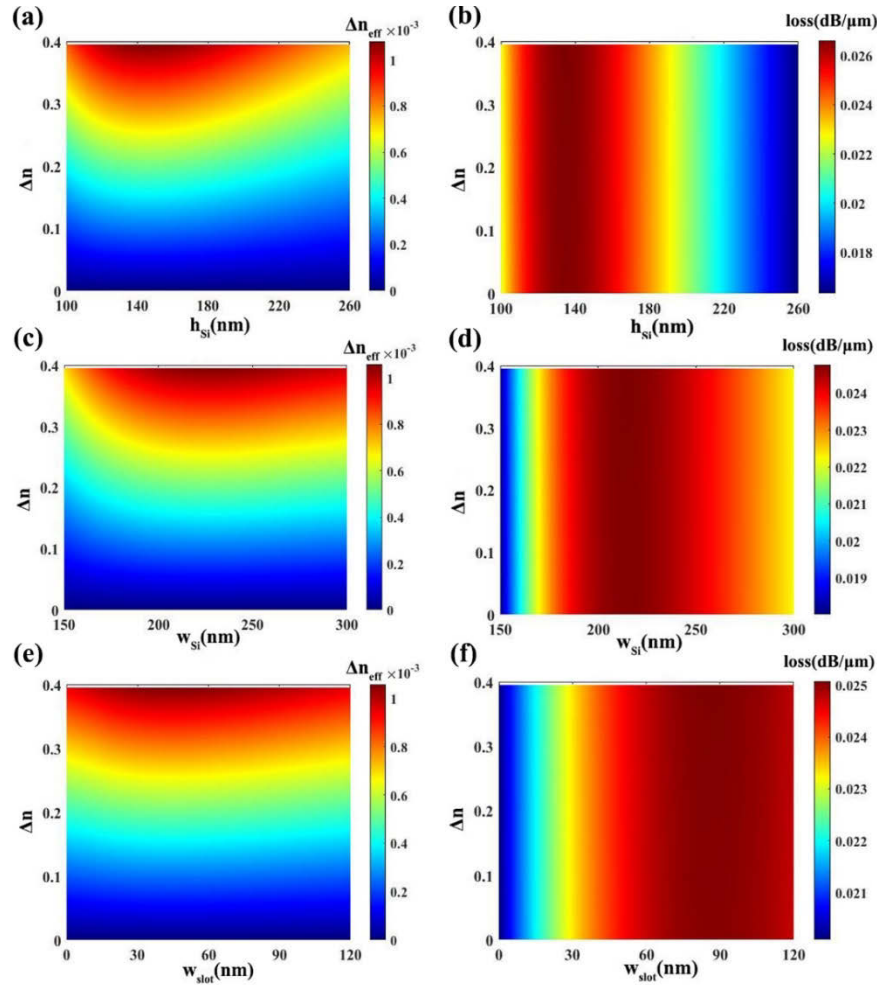


**Fig. 6.**  $\Delta \text{Re}(n_{\text{eff}})$  based on the TE polarization mode in the waveguide as a function of  $\Delta n$ , (a) silicon waveguide height  $h_{\text{Si}}$ , (c) silicon waveguide width  $w_{\text{Si}}$ , and (e) slot width  $w_{\text{slot}}$ . The loss as a function of  $\Delta n$ , (b) silicon waveguide height  $h_{\text{Si}}$ , (d) silicon waveguide width  $w_{\text{Si}}$ , and (f) slot width  $w_{\text{slot}}$ .

When  $h_{\text{Si}}$ ,  $w_{\text{Si}}$  and  $w_{\text{slot}}$  are 170, 210, and 30 nm, respectively, the relationship between  $\text{Re}(n_{\text{eff}})$  and loss with  $\Delta n$  is shown in Fig. 7(a). It can be seen from Fig. 7(a) that when the real part of the refractive index of MoSSe changes by 0.4,  $\text{Re}(n_{\text{eff}})$  changes by  $1.04 \times 10^{-3}$  and loss changes by 0.08%. In this case, as the refractive index increases, both  $\text{Re}(n_{\text{eff}})$  and loss exhibit an upward trend, and  $\text{Re}(n_{\text{eff}})$  changes significantly while the loss is small, which is appropriate for the phase modulation. The phase change of the modulator in Fig. 7(b) can be calculated using  $\Delta\varphi = 2\pi L \Delta \text{Re}(n_{\text{eff}}) / \lambda$ , where  $\lambda$  and  $L$  are the working wavelength and modulation length, respectively. With the modulation length  $L$  of 800  $\mu\text{m}$  and refractive index of MoSSe is changed by approximately 0.4 under an applied electric field, the phase change of the optical signal at a wavelength of 1550 nm after passing through the waveguide can effectively exceed  $\pi$ ; thus, the designed modulator performs satisfactorily.

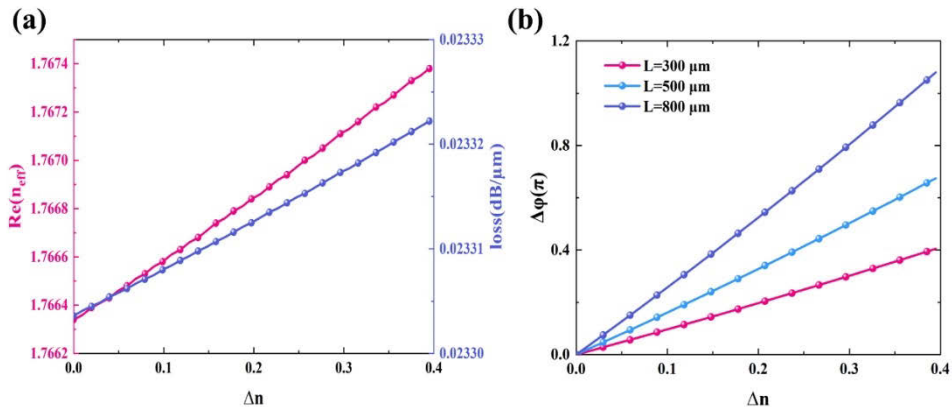


**Fig. 7.** (a) Loss and  $\text{Re}(n_{\text{eff}})$  of the modulator in the TE mode for different  $\Delta n$  in a monolayer MoSSe. (b) Phase change of the modulator with different length.

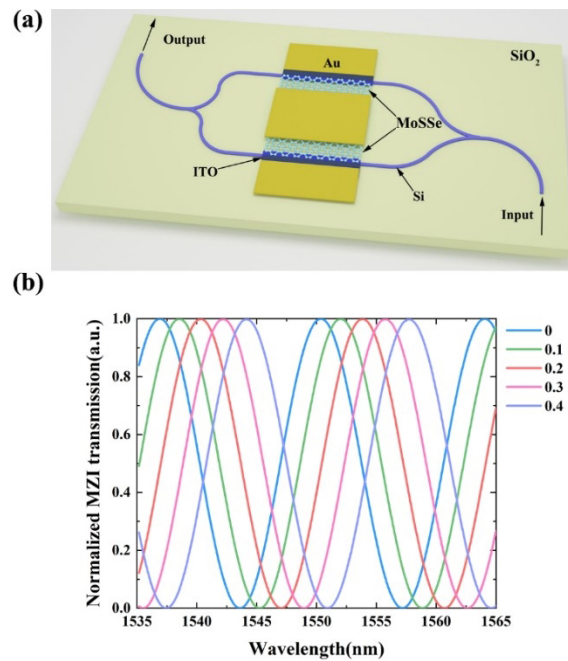


**Fig. 8.** (a) Schematic of MZM on the chip, the two arms of MZM are of unequal length, and patterned monolayer MoSSe on both arms exist. (b) The normalized transmission spectrum of the MZM with  $\Delta n$  from 0 to 0.4.

Figure 8(a) shows a schematic of the designed Mach-Zehnder modulator (MZM) with an imbalance length of 45  $\mu\text{m}$  between the two arms of MZM, on which an 800- $\mu\text{m}$ -long monolayer MoSSe film was formed, followed by deposition of metal electrodes. Figure 8(b) shows the interference pattern at the output of MZM in the TE mode, where applying different voltages on the long arms of MZM induces different amounts of refractive index change in the monolayer MoSSe. With an increase in  $\Delta n$ , the spectrum of MZM considerably shifts toward long wavelengths, as shown in Fig. 8(b), and the maximum shift exceeds 6 nm. In addition, MZM achieves a significant optical extinction at a wavelength of 1550 nm, which proves reasonable performance of the designed modulator. The efficiency of the modulator can be further improved by reducing the thickness of the spacer layer, changing the electrode material, and placing a single layer of material where the waveguide mode is maximized.

## 6. Conclusion

We prepared MoSSe dispersions using the liquid-phase exfoliation technique and characterized MoSSe using the Raman spectroscopy, absorption spectroscopy, and TEM. We studied the wavelength and pulse duration dependence of the SA response of MoSSe nanosheets under a 380-fs pulsed laser at 1040/520 nm and a 6-ns pulsed laser at 1064/532 nm using the open-aperture Z-scan technique, and subsequently calculated the GSA and ESA cross-sections using the fast and slow SA models. The results revealed that the NLO response of MoSSe in the visible light range is better than that of the near-infrared range, and it has a better NLO response ability under a 6-ns pulse than 380-fs pulse. Subsequently, we obtained the optical and electrical properties of MoSSe using the first-principles calculations. In addition, we combined MoSSe with an integrated photonic system to design and optimize a slot waveguide modulator operating at a wavelength of 1550 nm, and found that  $\text{Re}(n_{\text{eff}})$  can change by  $1.04 \times 10^{-3}$  and the loss does not change considerably, indicating that it is a phase modulator with a reasonable performance. Finally, the obtained results proved that MoSSe exhibits a reasonable nonlinear performance and an excellent potential for applications in integrated photonic devices.

**Funding.** Strategic Priority Research Program of Chinese Academy of Sciences (No. XDB43010303); National Natural Science Foundation of China (No. 61975221).

**Disclosures.** The authors declare no conflicts of interest.

**Data availability.** Data underlying the results presented in this paper are not publicly available at this time but may be obtained from the authors upon reasonable request.

**Supplemental document.** See [Supplement 1](#) for supporting content.

## References

1. Y. Qiao, X. Li, T. Hirtz, G. Deng, Y. Wei, M. Li, S. Ji, Q. Wu, J. Jian, F. Wu, Y. Shen, H. Tian, Y. Yang, and T. L. Ren, "Graphene-based wearable sensors," *Nanoscale* **11**(41), 18923–18945 (2019).
2. H. Zhan, D. Guo, and G. Xie, "Two-dimensional layered materials: From mechanical and coupling properties towards applications in electronics," *Nanoscale* **11**(28), 13181–13212 (2019).
3. B. Yao, Y. Liu, S.-W. Huang, C. Choi, Z. Xie, J. Flor Flores, Y. Wu, M. Yu, D.-L. Kwong, Y. Huang, Y. Rao, X. Duan, and C. W. Wong, "Broadband gate-tunable terahertz plasmons in graphene heterostructures," *Nat. Photonics* **12**(1), 22–28 (2018).
4. B. Yao, S. W. Huang, Y. Liu, A. K. Vinod, C. Choi, M. Hoff, Y. Li, M. Yu, Z. Feng, D. L. Kwong, Y. Huang, Y. Rao, X. Duan, and C. W. Wong, "Gate-tunable frequency combs in graphene-nitride microresonators," *Nature* **558**(7710), 410–414 (2018).
5. K. L. Seyler, P. Rivera, H. Yu, N. P. Wilson, E. L. Ray, D. G. Mandrus, J. Yan, W. Yao, and X. Xu, "Signatures of moire-trapped valley excitons in  $\text{MoSe}_2/\text{WSe}_2$  heterobilayers," *Nature* **567**(7746), 66–70 (2019).
6. J. Wu, H. Ma, P. Yin, Y. Ge, Y. Zhang, L. Li, H. Zhang, and H. Lin, "Two-dimensional materials for integrated photonics: Recent advances and future challenges," *Small Science* **1**(4), 2000053 (2021).
7. Y. Li, H. Chen, Y. Guo, K. Wang, Y. Zhang, P. Lan, J. Guo, W. Zhang, H. Zhong, Z. Guo, Z. Zhuang, and Z. Liu, "Lamellar hafnium ditelluride as an ultrasensitive surface-enhanced raman scattering platform for label-free detection of uric acid," *Photonics Res.* **9**(6), 1039–1047 (2021).

8. V. Soriano, M. Midrio, G. Contestabile, I. Asselberghs, J. Van Campenhout, C. Huyghebaert, I. Goykhman, A. K. Ott, A. C. Ferrari, and M. Romagnoli, "Graphene-silicon phase modulators with gigahertz bandwidth," *Nat. Photonics* **12**(1), 40–44 (2018).
9. M. Liu, X. Yin, E. Ulin-Avila, B. Geng, T. Zentgraf, L. Ju, F. Wang, and X. Zhang, "A graphene-based broadband optical modulator," *Nature* **474**(7349), 64–67 (2011).
10. M. A. Giambra, V. Miseikis, S. Pezzini, S. Marconi, A. Montanaro, F. Fabbri, V. Soriano, A. C. Ferrari, C. Coletti, and M. Romagnoli, "Wafer-scale integration of graphene-based photonic devices," *ACS Nano* **15**(2), 3171–3187 (2021).
11. M. Ono, M. Hata, M. Tsunekawa, K. Nozaki, H. Sumikura, H. Chiba, and M. Notomi, "Ultrafast and energy-efficient all-optical switching with graphene-loaded deep-subwavelength plasmonic waveguides," *Nat. Photonics* **14**(1), 37–43 (2020).
12. H. Wang, N. Yang, L. Chang, C. Zhou, S. Li, M. Deng, Z. Li, Q. Liu, C. Zhang, Z. Li, and Y. Wang, "CMOS-compatible all-optical modulator based on the saturable absorption of graphene," *Photonics Res.* **8**(4), 468–474 (2020).
13. E. Preciado, F. J. R. Schulein, A. E. Nguyen, D. Barroso, M. Isarraraz, G. von Son, I. H. Lu, W. Michailow, B. Moller, V. Klee, J. Mann, A. Wixforth, L. Bartels, and H. J. Krenner, "Scalable fabrication of a hybrid field-effect and acousto-electric device by direct growth of monolayer MoS<sub>2</sub>/LiNbO<sub>3</sub>," *Nat. Commun.* **6**(1), 8593 (2015).
14. S. Gan, C. Cheng, Y. Zhan, B. Huang, X. Gan, S. Li, S. Lin, X. Li, J. Zhao, H. Chen, and Q. Bao, "A highly efficient thermo-optic microring modulator assisted by graphene," *Nanoscale* **7**(47), 20249–20255 (2015).
15. X. Qiu, X. Ruan, Y. Li, and F. Zhang, "Multi-layer MOS capacitor based polarization insensitive electro-optic intensity modulator," *Opt. Express* **26**(11), 13902–13914 (2018).
16. E. J. Santos and E. Kaxiras, "Electrically driven tuning of the dielectric constant in MoS<sub>2</sub> layers," *ACS Nano* **7**(12), 10741–10746 (2013).
17. M. Romagnoli, V. Soriano, M. Midrio, F. H. L. Koppens, C. Huyghebaert, D. Neumaier, P. Galli, W. Templ, A. D'Errico, and A. C. Ferrari, "Graphene-based integrated photonics for next-generation datacom and telecom," *Nat. Rev. Mater.* **3**(10), 392–414 (2018).
18. Y. Ding, X. Zhu, S. Xiao, H. Hu, L. H. Frandsen, N. A. Mortensen, and K. Yvind, "Effective electro-optical modulation with high extinction ratio by a graphene-silicon microring resonator," *Nano Lett.* **15**(7), 4393–4400 (2015).
19. L. Zhuo, P. Fan, S. Zhang, Y. Zhan, Y. Lin, Y. Zhang, D. Li, Z. Che, W. Zhu, H. Zheng, J. Tang, J. Zhang, Y. Zhong, W. Fang, G. Lu, J. Yu, and Z. Chen, "High-performance fiber-integrated multifunctional graphene-optoelectronic device with photoelectric detection and optic-phase modulation," *Photonics Res.* **8**(12), 1949–1957 (2020).
20. J. Huang, N. Dong, S. Zhang, Z. Sun, W. Zhang, and J. Wang, "Nonlinear absorption induced transparency and optical limiting of black phosphorus nanosheets," *ACS Photonics* **4**(12), 3063–3070 (2017).
21. G. Wang, A. Chernikov, M. M. Glazov, T. F. Heinz, X. Marie, T. Amand, and B. Urbaszek, "Colloquium: Excitons in atomically thin transition metal dichalcogenides," *Rev. Mod. Phys.* **90**(2), 021001 (2018).
22. J. S. Ross, S. Wu, H. Yu, N. J. Ghimire, A. M. Jones, G. Aivazian, J. Yan, D. G. Mandrus, D. Xiao, W. Yao, and X. Xu, "Electrical control of neutral and charged excitons in a monolayer semiconductor," *Nat. Commun.* **4**(1), 1474 (2013).
23. K. F. Mak, K. He, C. Lee, G. H. Lee, J. Hone, T. F. Heinz, and J. Shan, "Tightly bound trions in monolayer MoS<sub>2</sub>," *Nat. Mater.* **12**(3), 207–211 (2013).
24. A. Chernikov, A. M. van der Zande, H. M. Hill, A. F. Rigosi, A. Velauthapillai, J. Hone, and T. F. Heinz, "Electrical tuning of exciton binding energies in monolayer WS<sub>2</sub>," *Phys. Rev. Lett.* **115**(12), 126802 (2015).
25. T. Zheng, Y. C. Lin, Y. Yu, P. Valencia-Acuna, A. A. Puretzky, R. Torsi, C. Liu, I. N. Ivanov, G. Duscher, D. B. Geohegan, Z. Ni, K. Xiao, and H. Zhao, "Excitonic dynamics in janus MoSSe and WSSe monolayers," *Nano Lett.* **21**(2), 931–937 (2021).
26. A. Y. Lu, H. Zhu, J. Xiao, C. P. Chuu, Y. Han, M. H. Chiu, C. C. Cheng, C. W. Yang, K. H. Wei, Y. Yang, Y. Wang, D. Sokaras, D. Nordlund, P. Yang, D. A. Muller, M. Y. Chou, X. Zhang, and L. J. Li, "Janus monolayers of transition metal dichalcogenides," *Nat. Nanotechnol.* **12**(8), 744–749 (2017).
27. L. Dong, J. Lou, and V. B. Shenoy, "Large in-plane and vertical piezoelectricity in janus transition metal dichalcogenides," *ACS Nano* **11**(8), 8242–8248 (2017).
28. H. Ma, Y. Zhao, Y. Shao, Y. Lian, W. Zhang, G. Hu, Y. Leng, and J. Shao, "Principles to tailor the saturable and reverse saturable absorption of epsilon-near-zero material," *Photonics Res.* **9**(5), 678–686 (2021).
29. M. Sheik-Bahae, A. A. Said, T. H. Wei, D. J. Hagan, and E. W. Van Stryland, "Sensitive measurement of optical nonlinearities using a single beam," *IEEE J. Quantum Electron.* **26**(4), 760–769 (1990).
30. K. Wang, J. Wang, J. Fan, M. Lotya, A. O'Neill, D. Fox, Y. Feng, X. Zhang, B. Jiang, Q. Zhao, H. Zhang, J. N. Coleman, L. Zhang, and W. J. Blau, "Ultrafast saturable absorption of two-dimensional MoS<sub>2</sub> nanosheets," *ACS Nano* **7**(10), 9260–9267 (2013).
31. L. Yang, R. Dorsinville, Q. Z. Wang, P. X. Ye, R. R. Alfano, R. Zamboni, and C. Taliani, "Excited-state nonlinearity in polythiophene thin films investigated by the z-scan technique," *Opt. Lett.* **17**(5), 323–325 (1992).
32. S. Delysse, J. M. Nunzi, and C. Scala-Valero, "Picosecond optical kerr ellipsometry determination of S<sub>1</sub>→S<sub>n</sub> absorption spectra of xanthene dyes," *Appl. Phys. B: Lasers Opt.* **66**(4), 439–444 (1998).
33. Z. Burshtein, P. Blau, Y. Kalisky, Y. Shimony, and M. R. Kikta, "Excited-state absorption studies of Cr<sup>4+</sup> ions in several garnet host crystals," *IEEE J. Quantum Electron.* **34**(2), 292–299 (1998).

34. M. Pokrass, Z. Burshtein, R. Gvishi, and M. Nathan, "Saturable absorption of multi-walled carbon nanotubes/hybrid-glass composites," *Opt. Mater. Express* **2**(6), 825–838 (2012).
35. S. Zhang, Y. Li, X. Zhang, N. Dong, K. Wang, D. Hanlon, J. N. Coleman, L. Zhang, and J. Wang, "Slow and fast absorption saturation of black phosphorus: Experiment and modelling," *Nanoscale* **8**(39), 17374–17382 (2016).
36. Y. Feng, N. Dong, G. Wang, Y. Li, S. Zhang, K. Wang, L. Zhang, W. J. Blau, and J. Wang, "Saturable absorption behavior of free-standing graphene polymer composite films over broad wavelength and time ranges," *Opt. Express* **23**(1), 559–569 (2015).
37. G. Wang, G. Liang, A. A. Baker-Murray, K. Wang, J. J. Wang, X. Zhang, D. Bennett, J.-T. Luo, J. Wang, P. Fan, and W. J. Blau, "Nonlinear optical performance of few-layer molybdenum diselenide as a slow-saturable absorber," *Photonics Res.* **6**(7), 674–680 (2018).
38. C. Chen, N. Dong, J. Huang, X. Chen, H. Wang, Z. Wang, and J. Wang, "Nonlinear optical properties and ultrafast carrier dynamics of 2D indium selenide nanosheets," *Adv. Opt. Mater.* **9**(24), 2101432 (2021).
39. X. Zhang, S. Zhang, C. Chang, Y. Feng, Y. Li, N. Dong, K. Wang, L. Zhang, W. J. Blau, and J. Wang, "Facile fabrication of wafer-scale MoS<sub>2</sub> neat films with enhanced third-order nonlinear optical performance," *Nanoscale* **7**(7), 2978–2986 (2015).
40. N. Mwankemwa, S. Chen, S. Gao, Y. Xiao, W. Zhang, and D. Zhu, "First-principles calculations to investigate the electronic and optical properties of (MoS<sub>2</sub>)<sub>4–n</sub>/(MoSSe)<sub>n</sub> lateral heterostructure," *J. Phys. Chem. Solids* **154**, 110049 (2021).
41. Z. H. Levine and D. C. Allan, "Linear optical response in silicon and germanium including self-energy effects," *Phys. Rev. Lett.* **63**(16), 1719–1722 (1989).
42. H. R. Philipp and H. Ehrenreich, "Optical properties of semiconductors," *Phys. Rev.* **129**(4), 1550–1560 (1963).
43. R. Kochar and S. Choudhary, "MoS<sub>2</sub>/phosphorene heterostructure for optical absorption in visible region," *IEEE J. Quantum Electron.* **54**(4), 1–6 (2018).
44. R. M. Martin, *Electronic structure: Basic theory and practical methods* (Cambridge university press, 2020).
45. N. R. Jungwirth and G. D. Fuchs, "Optical absorption and emission mechanisms of single defects in hexagonal boron nitride," *Phys. Rev. Lett.* **119**(5), 057401 (2017).
46. I. Datta, S. H. Chae, G. R. Bhatt, M. A. Tadayon, B. Li, Y. Yu, C. Park, J. Park, L. Cao, D. N. Basov, J. Hone, and M. Lipson, "Low-loss composite photonic platform based on 2D semiconductor monolayers," *Nat. Photonics* **14**(4), 256–262 (2020).
47. M.-S. Kwon, "Discussion of the epsilon-near-zero effect of graphene in a horizontal slot waveguide," *IEEE Photonics J.* **6**(3), 1–9 (2014).
48. Z. Liu, X. Li, C. Niu, J. Zheng, C. Xue, Y. Zuo, and B. Cheng, "56 Gbps high-speed Ge electro-absorption modulator," *Photonics Res.* **8**(10), 1648–1652 (2020).